

Supernova Remnants in the Magellanic Clouds. VI. The DEM L 316 Supernova Remnants

R. M. Williams & Y.-H. Chu

University of Illinois at Urbana-Champaign, 1002 W. Green St., Urbana, IL 61801 USA

rosanina@astro.uiuc.edu, chu@astro.uiuc.edu

ABSTRACT

The DEM L 316 system appears to contain two shells, both with the characteristic signatures of supernova remnants (SNRs). We have analyzed *Chandra* data for the two shells of DEM L 316, investigating its spatially resolved features at X-ray wavelengths. We confirm the findings of Nishiuchi et al. (2001) that the spectra of these shells are notably different, with Shell A requiring a high iron abundance for a good spectral fit. This implies an origin for Shell A in a Type Ia supernova, and separate progenitors for the two shells. We further explicitly find that the spectrum of Shell B requires much lower iron abundances, consistent with those typical of the local interstellar medium.

The two shells also show remarkable differences at smaller scales. Shell A shows a central X-ray brightening, similar to that seen in some “mixed morphology” remnants. Spectra of resolved regions for this SNR are quite similar, suggesting a high degree of internal mixing. The X-ray emission of Shell B is primarily in a broad annulus with brightest emission at its inner radius, particularly in one “knot” on this ring. Spatially resolved spectroscopy of this remnant suggests the presence of two temperature components within the bright ring and “knot”. We suggest that Shell B is an evolved SNR with material backfilling from the shell into the central cavity.

Subject headings: ISM: supernova remnants – ISM: individual (DEM L 316) – X-rays: ISM

1. Introduction

The peanut-shaped nebula DEM L 316 was first noted by Mathewson et al. (1983) to have the characteristics typical of supernova remnants (SNRs). A multi-wavelength study

by Williams et al. (1997) concluded that the most probable scenario for DEM L 316’s unique morphology was that it consisted of a pair of colliding SNRs. Evidence cited in support of this scenario included a change in radio polarization between the two shells, the kinematics of the two shells, multiwavelength morphological features and similar extinctions.

Alternate scenarios for the physical association of the two shells include (a) that the shells are the result of a single explosion into a bi-lobed cavity, or (b) that the shells are isolated SNRs apparently juxtaposed along the line of sight, but in fact spatially separated. Nishiuchi et al. (2001), using a study of combined *ROSAT* and *ASCA* X-ray data, noted that the shells were spectrally distinct to an extent which would rule out the single-explosion scenario, and also concluded that, on the basis of its enhanced iron abundance, Shell A was probably the result of a Type Ia SN.

In this paper, we present new *Chandra* observations of DEM L 316. These observations allow us, for the first time, to spatially resolve the structure of the DEM L 316 remnants, with reasonable spectral resolution over smaller regions. §2 describes our observations, while §3 contains our analysis. A discussion of the implications of our findings is given in §4, and those findings are summarized in §5.

2. Observations

We observed DEM L 316 with the *Chandra* Advanced CCD Imaging Spectrometer (ACIS) S3 back-illuminated chip (sequence number 500279, observation 2829, 40 ks). Data were reprocessed following procedures recommended by the Chandra X-ray Center (CXC): we removed the afterglow correction, generated a new bad pixel file, and applied corrections for charge-transfer inefficiency (CTI) and time-dependent gain for an instrument temperature of 120 K. We also applied background cleaning using the 5×5 pixel islands of our VFaint mode observation. The dataset was filtered for high-background times and poor event grades, resulting in a total “good time” interval of 35.6 ks, and restricted to the energy range of 0.3-8.0 keV, where the S3 chip is most sensitive.

Spectral results were extracted from the new event file. Background regions were taken from source-free areas surrounding the SNRs, and the spectrum of these background regions were scaled and subtracted from the source spectra. Individual spectra for regions of interest (Table 1), and the corresponding primary and auxiliary response files, were extracted with the CIAO *acispec* script and analyzed in XSPEC. Spectra were rebinned by spectral energy to achieve a signal-to-noise ratio of 3 in each bin.

Regions within DEM L 316 were chosen to examine specific morphological features seen

in our X-ray images (Figure 1 and Table 1). Regions 1 and 2 enclose the approximate X-ray boundaries of Shell A and Shell B, respectively. Region 3 covers the bright central emission within Shell A, while Region 4 includes the limb of Shell A, excluding that central emission. Regions 5-7 cover brighter X-ray “arcs” to the north, east, and south of Shell A; Region 8 samples emission between those arcs. In Shell B, Region 9 encloses the central emission from the remnant, and Region 10 covers a particularly bright “knot” of interior emission. Region 11 incorporates the ring-like structure of brighter emission in Shell B, including the “knot” of Region 10. Region 12 covers emission on the limb of Shell B, excluding the center and the ring.

For comparison, we utilized optical emission-line ($H\alpha$, [S II], [O III]) images taken with the Curtis-Schmidt telescope at Cerro Tololo Inter-American Observatory, and radio images from the Australia Telescope Compact Array at 4.4 and 6.0 GHz (7 and 5 cm). Details of these observations are given in Williams et al. (1997).

3. Results

3.1. X-ray Morphologies

Previous X-ray analyses have noted an X-ray separation between the shells of DEM L 316. Following the previous work, we designate the northeastern shell as Shell A, and the southwestern shell as Shell B. While we do see two distinct shells in the ACIS data, faint emission from the limb of Shell B appears to overlap Shell A. A three-color image comparing the *Chandra* morphology to emission in $H\alpha$ and 7 cm radio (Williams et al. 1997) is shown in Figure 2a. In general, the brightest regions of X-ray emission appear to correspond to areas that are fainter at radio wavelengths. Conversely, the X-rays grow fainter toward the radio-bright limbs. Similarly, the X-ray emission appears well-confined by the optical filaments along the limbs of both shells. In Shell A, some filaments across the face of the SNR appear to correspond roughly to regions of fainter X-ray emission, but there is no strong anticorrelation.

Shell A appears to have a bright ring of inner emission, as well as near-linear “arcs” extending outward from that ring. The southwestern side of the SNR is “flattened” somewhat toward Shell B, and appears slightly brighter on the flattened side. Notably, this flattening occurs just north of the apparent overlap between the two shells, running parallel to the optical filaments and radio-bright limb there. The bright inner X-ray emission is typical for “mixed morphology” SNRs, which have centrally filled X-ray emission and shell-like radio morphologies. In some cases, the central X-ray emission from mixed morphology SNRs takes

the form of an inner ring, similar to the one we see in Shell A (Rho & Petre 1998).

The faint, outermost emission from Shell B is somewhat irregular, and is elongated in the E-W direction. The primary source of this elongation seems to be an extension on the western side, which is matched by similar extensions in the optical and radio. The X-ray emission of Shell B is primarily in a broad X-ray annulus that matches the observed radio morphology well. At the inner radius of this annulus, there appears to be a brighter ring of inner emission, though this is not as prominent as that in Shell A. A bright X-ray knot is visible on the north side of this ring. Curiously, this knot is directly north of a “small-diameter source” noted in radio images by Williams et al. (1997).

To examine the morphology as a function of energy, we created a three-color image (Figure 2b) with emission divided into energy bands of 0.3-0.8 keV (soft), 0.8-1.5 keV (medium), and 1.5-8.0 keV (hard). The middle band was selected to show the contribution from the blend of Fe L lines that make up most of the X-ray emission in this energy range. The overall structure is similar in all three bands. Emission from Shell A shows considerably more medium-band emission than does Shell B; in particular, the central ring of Shell A is bright at these energies. In contrast, the X-ray knot in Shell B appears brightest in the hard band.

3.2. Spectral Fits

Thermal emission lines are clearly visible in the *Chandra* ACIS data for each of the remnants. We therefore investigated fits to thermal plasma models to determine the plasma parameters. To see whether the plasma in each SNR has reached ionization equilibrium, we fit non-equilibrium ionization (NEI) models to the spectrum of each spatially-selected region, modified by photoelectric absorption. Abundances for each model are given as fractions of the solar abundance values of Anders & Grevesse (1989).

Specifically, we used a plane-parallel shock model (“vpshock” in XSPEC)¹. The model parameters are the mean shock temperature kT , ionization timescale τ ($=n_e t_{\text{ion}}$), elemental abundances, and a normalization A proportional to the distance and volume emission measure ($A(\text{cm}^{-5}) = 10^{-14} \int n_e n_H dV / 4\pi D^2$). Here, n_e is the electron density, n_H the hydrogen density, t_{ion} the shock age (time since the earliest material was shocked), V the volume occupied by the hot gas, and D the distance, all in cgs units.

¹Details and references for the vpshock model can be found at <http://heasarc.gsfc.nasa.gov/docs/xanadu/xspec/manual/node40.html>.

3.2.1. Comparison of the two shells

We extracted spectra from regions covering all of Shell A and all of Shell B (Table 1, Regions 1-2). The fitted spectral parameters are given in Table 2. It was not possible to obtain a statistically acceptable fit to both shell spectra with the same model parameters.

The absorption column densities were consistent with a value of $3.4 \pm 0.2 \times 10^{21}$ H-atom cm^{-2} over both shells, for a range of model combinations. This value is reasonably consistent with the estimate of 3.8×10^{21} cm^{-2} found from H I data in Williams et al. (1997). Data from a more recent H I survey of the LMC gives a higher figure of 6.2×10^{21} cm^{-2} (Staveley-Smith et al. 2003; Kim et al. 2003) within the LMC toward DEM L 316, which, when added to the Galactic foreground of 5×10^{20} cm^{-2} (Schwering & Israel 1991), gives a higher value of 6.7×10^{21} cm^{-2} . Note that the H I estimates include contributions from gas behind DEM L 316. Conversely, contributions to X-ray absorption from molecular gas will not be accounted for in H I.

Shell A is well fit by a single vps shock component (modified by photoelectric absorption) with high iron abundance. Acceptable fits could be achieved with iron abundances between 1 and 5 times solar values of Anders & Grevesse (1989); in all cases, substantially above the mean LMC abundance for iron. The best fit model yields an absorbed 0.3–8.0 keV flux of $6 \pm 2 \times 10^{-13}$ $\text{erg cm}^{-2} \text{ s}^{-1}$, an unabsorbed flux of $2 \pm 1 \times 10^{-12}$ $\text{erg cm}^{-2} \text{ s}^{-1}$, and a luminosity of $3 \pm 2 \times 10^{35}$ erg s^{-1} . The upper limit on an additional power-law component is an absorbed flux of 1×10^{-14} $\text{erg cm}^{-2} \text{ s}^{-1}$, or 1.7% of the total flux; inclusion of such a component, however, does not improve the fit.

Shell B does not require iron abundances above the LMC mean value; models including an iron abundance of 1.0 solar or above could be ruled out at the 90% confidence level. However, a single vps shock component provides only a poor fit, with an unusually high temperature (> 3 keV) for a large, X-ray faint SNR. A substantial improvement in the fit is possible by using two components - either a combination of vps shock and power-law models or two vps shock models with the same abundances. The former gives acceptable fits for values of the photon index Γ in the 1.6-1.8 range, somewhat flatter than typical for SNRs. The 0.3-8 keV flux for this model is 1×10^{-12} $\text{erg cm}^{-2} \text{ s}^{-1}$ (3×10^{-12} $\text{erg cm}^{-2} \text{ s}^{-1}$ unabsorbed), implying a luminosity of 4×10^{35} erg s^{-1} . The power-law component takes up 53% of the absorbed flux.

The two-plasma fit gives an ionization-equilibrium component with a temperature ~ 0.5 keV, and a non-equilibrium component with $kT > 5$ keV. The fitted abundances are close to typical LMC abundances. The fluxes and luminosities for this model fit are the same, to one significant figure, as those for the combined plasma/power-law fit. In this case the

high-temperature component accounts for 66% of the flux.

3.2.2. *Regions within the SNR*

We fitted the spectral model found for Shell A to the various sub-regions within Shell A (Regions 3-8). For most regions (3-6,8) the emission did not significantly deviate from this model, and a joint fit (with only normalizations varied) produced statistically acceptable results. The exception was the S Arc region (Region 7), along the “flattened” side of the SNR. Emission from this region had an excess of soft emission when compared to the best-fit model for Shell A, and the joint fit to Shell A and the S Arc was poor. If we assume the abundances to be the same for this region as for Shell A generally, the S Arc region requires a slightly higher temperature ($kT \sim 1.5$) and lower ionization parameter for a good fit.

Similarly, we used the two-plasma fit to Shell B to perform joint fits with Shell B and its sub-regions (Regions 9-12). All of these regions were well described by the overall two-plasma-component Shell B fit, although the relative normalizations of the two components differ. The high temperature component accounted for $> 70\%$ of the unabsorbed flux for the Hard Knot (Region 10), $\sim 40\%$ of the flux for the Center Ring (Region 11) and $< 30\%$ of the flux in the Limb and Faint Center (Regions 9 and 12).

We attempted to obtain additional information from these spatially resolved regions by fitting their spectra individually. To reduce the number of free parameters, we fixed the absorption column density to the average value found for Shells A and B above, and fixed all plasma abundances except iron to 30% of their solar values. Given the low number of counts in most regions, it is unsurprising that the fits are highly uncertain, as seen from the broad errors on each fitted parameter.

For all of these regions, a simple power-law fit alone could be ruled out at or above the 90% confidence level. The best power-law fit, though still not statistically acceptable, was to the data from the “Hard Knot” region of Shell B (Table 1, Region 10). As with Shell B overall, an acceptable fit to the “Hard Knot” region could be obtained with a combination of plasma and power-law, or two plasma models at different temperatures.

Broadly, the spectra of various regions within Shell A are quite similar. The temperatures are consistently within the range of 0.9-1.2 keV, and the fitted iron abundance within the range of 1.0-1.7 times solar values. The discrepancy between our fitted values for Fe abundance in the entire Shell A and sub-sections of this shell appears to be due to the difference in fitting procedure. For Shell A itself, we allowed Mg, Si, S and Fe to vary, while for the sub-regions we only allowed Fe to vary. When we fix all abundances except Fe at

0.3 for Shell A, we obtain Fe abundances of 1.7 ± 0.2 solar. Allowing the S abundance, for example, to vary freely leads to a significant improvement of the fit (F-test probability for no improvement of 0.08) and a larger Fe abundance. The greatest differences between spectral fits to the various regions appears to be in the ionization timescale τ , which is lower in regions along the remnant limb than toward the center. If we assume that most of the bright X-ray emitting gas is recently shocked, this would imply an increase in density toward the bright central region.

For Shell B, the temperatures of the best-fit model combinations are generally in the 0.6-0.8 keV range, with iron abundances less than 40% of solar values. The bright ring of emission is set apart from other areas of Shell B in requiring a high temperature or a second spectral component to provide an acceptable fit.

3.2.3. Shell Properties

The fitted parameters for the NEI plane-shock spectral models can be used to derive a number of physical properties for the SNRs. For this purpose we assume that hydrogen and helium are fully ionized, and that $n_{\text{He}}/n_{\text{H}} = 0.1$; thus, the total particle density is about $1.92n_{\text{e}}$. We assume each SNR to be an ellipsoid with the line-of-sight dimension equal to the length of the semiminor axis, with volume V and hot gas volume filling factor f_{hot} .

The spectrum of Shell A is reasonably consistent throughout the remnant, and can be well described by a single spectral component. We therefore use the overall spectral fit to Shell A as the basis for our estimation of its physical properties. For Shell B, the picture is complicated by the likely presence of more than one spectral component, and by variations over the face of the remnant. To characterize the properties of its overall expansion, therefore, we use the single-component spectral fit to the limb region (Region 12) as the basis for our calculations. From the normalization factor for a fitted spectrum, we can estimate the electron density and mass of the hot gas by:

$$n_{\text{e}} = 3.89 \times 10^7 DA^{1/2} V^{-1/2} f_{\text{hot}}^{-1/2} \text{ cm}^{-3}$$

$$M_{\text{gas}} = 1.17 n_{\text{e}} m_{\text{H}} V f_{\text{hot}} \text{ g}$$

The density and the plasma temperature (here given in keV) can be used to derive the thermal energy and pressure of the hot gas, according to:

$$E_{\text{th}} = 4.60 \times 10^{-9} n_e T_{\text{keV}} V f_{\text{hot}} \text{ erg}$$

$$P_{\text{th}} = 3.05 \times 10^{-9} n_e T_{\text{keV}} \text{ dyn cm}^{-2}$$

In addition, by presuming the plasma to be heated to the shock temperature, we can calculate a shock velocity in km s^{-1} of

$$v_{\text{shock}} = 913 T_{\text{keV}}^{1/2}$$

Assuming adiabatic (Sedov) expansion, we can presume the expansion velocity $v_{\text{exp}} = 3/4 v_{\text{shock}}$. The age of a remnant can be calculated from its expansion from $t = \eta R / v_{\text{exp}}$, where η depends on the evolutionary stage of the SNR ($\eta = 0.4$ for Sedov expansion). This gives a dynamical age:

$$t_{\text{dyn}} = 1.23 \times 10^{13} R_{\text{pc}} / v_{\text{exp}}$$

where R_{pc} is the SNR radius in parsecs. For these shells, we used an average radius for the dynamical age estimate. Results of these calculations are shown in Table 5. Note that the properties dependent on n_e are affected by our choice of volume filling factor; this factor is therefore included in the numbers cited in Table 5. Quoted errors are simply propagation of errors in fitted parameters and volumes, and do not take into account uncertainties due to the choice of spectral models and filling factor.

4. Discussion

4.1. Abundances and SNR Types

We are able to confirm the striking difference, first analyzed by Nishiuchi et al. (2001), between the spectra of the two shells of DEM L 316. One notable feature of this difference is that the spectrum for Shell A requires an iron abundance significantly higher than that typical for the LMC in order to fit the spectrum, while no such condition is required for (or indeed permitted by) the spectrum of Shell B.

The iron abundance found for Shell A, of three times solar abundances, is somewhat higher than the value of ~ 1.9 solar found by Nishiuchi et al. (2001). However, as discussed in

§3.2.2, we can attribute this difference to the differing methods of spectral analysis. The fits of Nishiuchi et al. (2001) fixed all elemental abundances except Ne and/or Fe to the mean LMC values of 0.3 solar. When we use the same procedure in fitting the spectrum of Shell A, the fitted Fe abundances of 1.7 ± 0.2 solar are within the error range of the Nishiuchi et al. (2001) value.

The abundances found for Shell B are all well below the solar values, and in most cases near their typical LMC values (Russel & Dopita 1992). Our values for the iron abundance in the entire Shell B, and for sub-sections of this shell, all fall within the range of 0.16-0.4 solar. Nishiuchi et al. (2001) did not fit the Fe value directly for this shell, but noted that a fit with a fixed Fe abundance of 0.3 solar provided a reasonable spectral fit. These low abundance values suggest that the SNR is dominated by emission from swept-up material, so that the contributions of ejecta enrichment from this SNR are largely undetectable.

The inferred presence of significant iron ejecta within a SNR is frequently used to suggest that the SNR resulted from a Type Ia explosion (e.g., Hendrick, Borkowski, & Reynolds 2003; Nishiuchi et al. 2001; Hughes et al. 1995). Theoretical models (e.g., Badenes et al. 2003; Iwamoto et al. 1999) of Type Ia SNe and their remnants predict substantially higher ratios of Fe to other elements than those seen in remnants of Type II SNe. Although the oxygen abundance cannot be constrained sufficiently to obtain the revealing [O/Fe] ratio, the unusually high iron abundance, particularly when contrasted with the less-enhanced Mg and Si, seems to class Shell A among LMC SNRs such as 0548-70.4 and 0534-69.9 (Hendrick, Borkowski, & Reynolds 2003) and DEM L 71 (Hughes et al. 2003), which are tentatively classed as remnants of Type Ia SNe due to high iron abundances. (0548-70.4 and DEM L 71 also have Balmer-line dominated optical emission, a classic signature of a Type Ia remnant.) We therefore agree with the conclusion of Nishiuchi et al. (2001) that Shell A is probably a remnant of a Type Ia SN, and Shell B is likely to be a remnant of a Type II SN.

With regards to the central assertion of Williams et al. (1997) that DEM L 316 consists of a pair of colliding SNRs, the verdict of the new findings is mixed. As suggested by Nishiuchi et al. (2001), we can decisively rule out the hypothesis that this system is the result of a single explosion into a bi-lobed cavity, on the basis of the wholly different heavy element abundances found for the two shells. The case for the collision of the two SNRs, however, is somewhat weakened by the tentative conclusion that Shell A is the remnant of a Type Ia SN. The explosions of two massive stars within the short lifetime of a SNR is conceivable if the two were members of a loose association; however, if one SNR is Type Ia, no such association can be established.

SNRs from Type Ia SNe may of course be seen occasionally in proximity to massive-star phenomena. For example, the LMC SNR N103B shows X-ray inferred abundances that

suggest a type Ia origin (Lewis et al. 2003; Hughes et al. 1995), though this conclusion is disputed (van der Heyden et al. 2002). This SNR is located at the periphery of H II region DEM L 84, and is within 40 pc of the NGC 1850 superbubble and its population of massive stars (Chu & Kennicutt 1988). However, the observable lifetime of a SNR is relatively short (e.g., Slavin & Cox 1992), and therefore the probability of two independent SNe from non-associated progenitors within that lifetime is low. Thus, such a collision must be presumed to be a rare event, and the chances of observing it small.

4.2. SNR Physical Properties

Many of the properties listed in Table 5 are dependent on the volume filling factor f_{hot} . For classical spherical Sedov expansion, we would expect a shell thickness of 1/12 the radius, giving $f_{\text{hot}} \approx 0.25$. Using this value, we find electron densities of 0.4 ± 0.1 for Shell A, and 0.3 ± 0.1 for Shell B. These densities are consistent with the broad ranges found by Williams et al. (1997) from *ROSAT* data. The electron density found for Shell A is also consistent, within the errors, with the ion density (presumed equal to the electron density) found by Nishiuchi et al. (2001) from *ASCA* spectra, although it should be noted that their derived density was based on a value of $f_{\text{hot}} = 1$ for this shell. If we similarly presumed $f_{\text{hot}} = 1$ to reflect the filled morphology, our density is only 0.2 ± 0.1 for Shell A. For Shell B, the value we find from the SNR limb is somewhat lower than that found by Nishiuchi et al. (2001); this difference is unsurprising, given that their spectral fit covered the entire remnant.

The thermal energies for the hot gas, using $f_{\text{hot}} \approx 0.25$, are $1.1 \pm 0.1 \times 10^{50}$ erg and $1.8 \pm 0.2 \times 10^{50}$ erg for Shells A and B, respectively. These values are also within the broad ranges found by Williams et al. (1997). The pressures found with this filling factor are $1.4 \pm 0.7 \times 10^{-9}$ dyn cm $^{-2}$ for Shell A and $7.8 \pm 0.8 \times 10^{-10}$ dyn cm $^{-2}$ for Shell B, somewhat higher than the *ROSAT*-derived values. We attribute this to the higher temperature (or high-temperature component) found from *Chandra* data; it is unsurprising that *ROSAT*, sensitive in the 0.2-2.4 keV range, would not have provided sufficient information at the high-energy end of the spectrum for accurate temperature determinations. (However, note that a higher filling factor for Shell A can lower the presumed pressure.) Our findings reinforce the conclusion of Williams et al. (1997) that the hot gas thermal pressure exceeds the sum of the magnetic pressure and the thermal pressure in the warm ionized gas seen in optical emission lines.

The ages of the SNRs are a somewhat perplexing question. If the relatively high temperatures found in the X-ray gas are produced at the forward shock, and the SNRs are undergoing Sedov expansion, then the high expansion velocities inferred from the X-ray tem-

peratures imply ages of 7,400 yr for Shell A and 13,000 yr for Shell B (Table 5). However, the centrally brightened X-ray morphology of Shell A and the multiple shock components of Shell B suggest that such assumptions for the shock structure are overly simplistic; these values might better be considered as lower limits on the shell ages. In contrast, using expansion velocities measured from echelle spectroscopy, and assuming Sedov expansion, Williams et al. (1997) found ages of 27,000 yr and 39,000 yr for Shells A and B, although the authors state that the highest-velocity material may not have been detected.

Using the ionization timescale from their X-ray spectral fits, Nishiuchi et al. (2001) estimated ages of $\sim 39,000$ yr for Shell A, and $> 42,000$ yr for Shell B, based on filling factors of $f_{\text{hot}} = 1$ for Shell A and 0.25 for Shell B. Using $f_{\text{hot}} = 1$, our ionization timescales and derived densities give an age of 46,000 yr for Shell A; a Sedov filling factor of 0.25 gives 23,000 yr. This broad range is quite consistent with the previous estimates of Williams et al. (1997) and Nishiuchi et al. (2001). In the case of Shell B, our estimates are complicated by the presence of multiple spectral components. Using only the outer limb region, the ionization timescale yields an age of only 17,000 yr for $f_{\text{hot}} = 0.25$. This age, however, contradicts our expectation that the larger, fainter shell should be the older of the two, given similar interstellar environments. In part, we can consider the ionization timescale for Shell B as only a rough estimate, given the range of ionization timescales for various regions within this SNR. If we do consider the estimate to be reliable, one possible explanation for such a discrepancy might be the expansion of the Shell B SNR within a cavity carved by the massive-star progenitor, which could allow it to reach a large size in its early expansion (Chevalier & Liang 1989). Shell A, as a remnant of a Type Ia SN, would not be expected to have had such a low-density environment.

4.3. The Nature of the Two SNRs

The central X-ray brightening of Shell A, in the context of its limb brightened radio emission, suggests it can be classified as a “mixed morphology” SNR. Spectra of resolved regions for this SNR are remarkably similar in temperatures and abundances. These similarities can be accounted for by a high degree of internal mixing. This is consistent with recent models of mixed morphology remnants, which suggest that “entropy mixing” (which includes turbulent mixing and/or thermal conduction) may play a large part in the morphological features of such remnants (e.g., Shelton, Kuntz, & Petre 2004; Shelton et al. 1999). Notably, in the mixed-morphology SNR W44 and others, the central plasma is thought to be “near collisional ionization equilibrium” (CIE; Shelton, Kuntz, & Petre 2004); if we use the characteristic $n_e t_{eq} \approx 10^{12} \text{ cm}^{-3} \text{ s}$ (Masai 1994) then the central emission of Shell A shares

this characteristic as well.

The identification of Shell A as a Type Ia SN is in interesting contrast to its apparent mixed morphology. Mixed-morphology SNRs are generally seen in the vicinity of molecular clouds (Rho & Petre 1998, and references therein), as seen for example in their association with maser activity (e.g., Yusef-Zadeh et al. 2003). Several mixed-morphology SNRs also contain pulsars or PWN (e.g., Williams et al. 2005; Shelton, Kuntz, & Petre 2004; Rho et al. 1994). Thus, mixed-morphology SNRs are usually associated with massive-star phenomena. However, the case of N103B cited above (§4.1) shows that SNRs from Type Ia SNe may be located in regions of substantial massive-star activity. In addition, N103B is brightened in radio and optical toward the N103 H II region, suggesting interaction of the shock with dense material (e.g., Dickel & Milne 1995, and references therein). A plausible explanation for the mixed morphology of Shell A, therefore, may be that it is situated in a relatively dense environment.

Shell B has, in most respects, the characteristics of an older shell-type remnant. Abundance values are similar to those typical of the LMC ISM, suggesting that the SNR is dominated by emission from swept-up material. The X-ray emission is not limb-brightened as one expects for young SNRs, although the X-ray emission does not appear notably enhanced toward the center as with mixed morphology SNRs. The low surface brightness of the X-ray emission and relatively slow expansion velocity are also consistent with this picture.

Perhaps the most notable feature within Shell B is the “Hard Knot” of brighter X-ray emission. Given its proximity to the “small diameter radio source” mentioned in Williams et al. (1997), it is tempting to speculate that the hard emission may come from a pulsar-wind nebula (PWN) embedded within the thermally-emitting shocked material. However, the X-ray peak is offset from the radio peak by $13''$, greater than can be accounted for by the radio half-power beam width of $12''$. A search of the X-ray power spectrum shows no evidence for periodic emission; this is unsurprising, as the 3.2 second timing resolution of *Chandra*’s ACIS is insufficient to detect the pulsations from a typical pulsar.

Perhaps a more likely possibility is that this “Hard Knot” is a clump of dense material well behind the SNR shock front. The knot appears to be one of several less-prominent knots that make up the “Bright Ring” of X-ray emission within the SNR. This ring, in turn, appears to coincide with the inner edge of the thick shell seen at radio wavelengths. If this material is evaporating into the hot cavity within the SNR, it could raise the surface brightness of high-temperature gas shocked during more energetic phases of the SNR’s expansion (e.g., White & Long 1991). The high ionization timescales found for the “Hard Knot” are consistent with a high density in this clump.

5. Summary

Chandra ACIS images and spectra reveal new details of the DEM L 316 SNRs. We are able to confirm the findings of Nishiuchi et al. (2001) that the spectrum of Shell A requires a high iron abundance, and thus that this SNR likely resulted from a Type Ia SN. We are able to extend their work by explicitly fitting abundances for Shell B, showing that a high iron abundance would provide a poor fit in this case. This strengthens the argument of Nishiuchi et al. (2001) that the shells are spectrally distinct and thus not part of a single bipolar shell.

We further analyze the morphology and spatially-resolved spectroscopy for the two SNRs. We find that Shell A has many of the characteristics of “mixed morphology” SNRs, including centrally concentrated X-ray emission within a radio shell, a homogenous temperature distribution, and central emission in ionization equilibrium. Shell B, in contrast, appears fairly typical of an evolved shell-type SNR. A bright knot of harder X-rays within the SNR appears to be part of an interior ring of X-ray emission. We suggest that this ring is produced by the backfilling of a thick shell into the hot, low-density cavity of the SNR.

The authors thank the anonymous referee for comments which have helped to improve this paper. RMW acknowledges support from SAO grant GO2-3096A and NASA grant LTSA04-0000-0043.

REFERENCES

- Anders, E. & Grevesse, N. 1989, *Geochimica et Cosmochimica Acta* 53, 197
- Badenes, C., Bravo, E., Borkowski, K. J., & Domnguez, I. 2003, *ApJ*, 593, 358
- Chevalier, R. A., & Liang, E. P. 1989, *ApJ*, 344, 332
- Chu, Y.-H. & Kennicutt, R. C., Jr. 1988, *AJ*, 96, 1874
- Dickel, J. R., & Milne, D. K. 1995, *AJ*, 109, 200
- Haberl, F. & Pietsch, W. 1999, *A&AS*, 139, 277
- Hendrick, S. P., Borkowski, K. J., & Reynolds, S. P. 2003, *ApJ*, 593, 370
- Hughes, J. P. et al. 2003, *ApJL*, 582, 95
- Hughes, J. P. et al. 1995, *ApJL*, 444, 81

- Ikeuchi, S. 1978, PASJ, 30, 563
- Iwamoto, K., Brachwitz, F., Nomoto, K., Kishimoto, N., Umeda, H., Hix, W. R., & Thielemann, F. 1999, ApJS, 125, 439
- Kim, S., Staveley-Smith, L., Dopita, M. A., Sault, R. J., Freeman, K. C., Lee, Y., & Chu, Y.-H. 2003, ApJS, 148, 473
- Lewis, K. T., Burrows, D. H., Hughes, J. P., Slane, P. O., Garmire, G. P., & Nousek, J. A. 2003, ApJ, 582, 770
- Masai, K. 1994, ApJ, 437, 770
- Mathewson, D. S., Ford, V. L., Dopita, M. A., Tuohy, I. R., Long, K. S., & Helfand, D. J. 1983, ApJS, 51, 345
- Nishiuchi, M., Yokugawa, J., Koyama, K., & Hughes, J.P. 2001, PASJ, 53, 99
- Park, S. et al. 2003, ApJ, 586, 210
- Rho, J. & Petre, R. 1998, ApJL, 503,167
- Rho, J., Petre, R., Schlegel, E. M., & Hester, J. J. 1994, ApJ, 430, 757
- Russel, S. C. & Dopita, M. A. 1992, ApJ, 384, 508
- Schwering, P. B. W., & Israel, F. P. 1991, A&A, 246, 231
- Shelton, R. L., Kuntz, K. D., & Petre, R. 2004, ApJ, 611, 906
- Shelton, R. L. et al. 1999, ApJ, 524, 192
- Slavin, J. D. & Cox, D. P. 1992, ApJ, 392, 131
- Staveley-Smith, L., Kim, S., Calabretta, M. R., Haynes, R. F., & Kesteven, M. J. 2003, MNRAS, 339, 87
- van der Heyden, K. J., Behar, E., Vink, J., Rasmussen, A. P., Kaastra, J. S., Bleeker, J. A. M., Kahn, S. M., & Mewe, R. 2002, A&A, 392, 955
- White, R. L., & Long, K. S. 1991, ApJ, 373, 543
- Williams, R. M., Chu, Y.-H., Dickel, J. R., Beyer, R., Petre, R., Smith, R. C., & Milne, D. K, 1997, ApJ, 480, 618

Williams, R. M., Chu, Y.-H., Dickel, J. R., Gruendl, R. A., Seward, F. D., Guerrero, M. A.
& Hobbs, G. 2005, ApJ, astro-ph/0504609

Yusef-Zadeh, F., Wardle, M., Rho, J., & Sakano, M. 2003, ApJ, 585, 319

Table 1. Spatial regions used for spectral fits

	SNR	Region	Counts ^a	Center (J2000 RA, Dec)	radii (")
1	Shell A	entire SNR	6352 ± 91	05:47:21.4, –69:41:28	63, 49
2	Shell B	entire SNR	7085 ± 140	05:46:58.8 –69:43:00	104, 64
3	Shell A	Bright Center	2822 ± 56	05:47:19.0 –69:41:33	21
4	Shell A	Limb ^b	3024 ± 85	05:47:21.4, –69:41:28	63, 49 –25
5	Shell A	N Arc	737 ± 31	05:47:16.9 –69:40:58	36, 8
6	Shell A	E Arc	460 ± 24	05:47:26.3 –69:41:16	19, 8
7	Shell A	S Arc	480 ± 26	05:47:19.8 –69:42:10	32, 8
8	Shell A	faint	576 ± 31	05:47:22.0 –69:40:58	15 (N)
				05:47:24.2 –69:41:53	15 (S)
9	Shell B	Faint Center	317 ± 22	05:47:02.8 –69:42:55	15
10	Shell B	Hard Knot	711 ± 29	05:46:58.9 –69:42:27	14
11	Shell B	Center Ring ^b	3555 ± 79	05:47:02.2 –69:42:54	46 –16
12	Shell B	Limb ^b	2714 ± 112	05:46:58.8 –69:43:00	104, 64 –49

^aBackground-subtracted counts in the 0.3-8 keV range, over 35585 s exposure time.

^bRegion with central emission excluded; radius of excluded region given as -X.

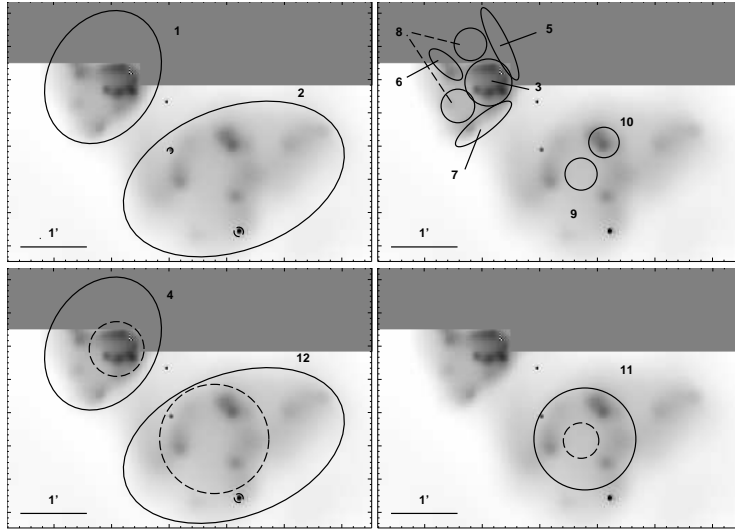


Fig. 1.— Adaptively smoothed *Chandra* ACIS image with spectral regions marked and labeled as listed in Table 1. Regions with dotted lines are excluded from larger regions.

Table 2. Best-fit spectral models to SNR shells

Parameter	Shell A		Shell B			
component	vpshock	vpshock	vpshock + power-law		vpshock + vpshock	
N_H (cm $^{-2}$)	$3.6^{+0.2}_{-0.3} \times 10^{21}$	$3.6^{+0.1}_{-0.2} \times 10^{21}$	$3.1^{+0.1}_{-0.3} \times 10^{21}$		$2.6^{+0.2}_{-0.2} \times 10^{21}$	
kT (keV)	$1.1^{+0.1}_{-0.1}$	$3.7^{+0.7}_{-0.6}$	$0.47^{+0.03}_{-0.04}$...	$0.55^{+0.3}_{-0.4}$	9^{+1}_{-2}
O/O $_{\odot}$	0.3 ^a	$0.21^{+0.03}_{-0.02}$	$0.42^{+0.07}_{-0.07}$...	$0.26^{+0.04}_{-0.05}$	
Ne/Ne $_{\odot}$	0.3 ^a	$0.25^{+0.04}_{-0.09}$	$0.6^{+0.1}_{-0.1}$...	$0.3^{+0.1}_{-0.1}$	
Mg/Mg $_{\odot}$	$0.9^{+0.2}_{-0.2}$	$0.38^{+0.08}_{-0.06}$	$0.37^{+0.09}_{-0.09}$...	$0.46^{+0.09}_{-0.08}$	
Si/Si $_{\odot}$	$1.0^{+0.3}_{-0.2}$	$0.2^{+0.2}_{-0.1}$	$0.4^{+0.2}_{-0.3}$...	$0.4^{+0.1}_{-0.2}$	
S/S $_{\odot}$	2^{+1}_{-1}	0.3 ^a	0.3 ^a	...	0.3 ^a	
Fe/Fe $_{\odot}$	$3.0^{+0.5}_{-0.2}$	$0.39^{+0.05}_{-0.03}$	$0.16^{+0.03}_{-0.02}$...	$0.24^{+0.06}_{-0.03}$	
τ (cm $^{-3}$ s)	$2.8^{+0.2}_{-0.2} \times 10^{11}$	$2.9^{+0.3}_{-0.3} \times 10^{10}$	$6^{+7}_{-3} \times 10^{12}$...	$< 5 \times 10^{13}$	$8^{+2}_{-2} \times 10^{10}$
Γ	$1.5^{+0.1}_{-0.4}$
norm (cm $^{-5}$)	$2.30^{+0.05}_{-0.06} \times 10^{-4}$	$6.2^{+0.2}_{-0.1} \times 10^{-4}$	$1.91^{+0.07}_{-0.05} \times 10^{-3}$	$9.1^{+0.9}_{-0.9} \times 10^{-5}$	$9.9^{+0.1}_{-0.4} \times 10^{-4}$	$3.3^{+0.1}_{-0.2} \times 10^{-4}$
χ^2_{red}	1.19	1.29		1.09		1.08
dof	210	348		346		345

Note. — Spectra cover the range between 0.3-8.0 keV. Elements not listed are fixed to the LMC mean abundance (Russel & Dopita 1992). Errors are the statistical errors in each fit parameter at the 90% uncertainty level.

^aCould not be adequately constrained, so fixed to LMC mean abundance.

Table 3. Best-fit spectral models to regions in Shell A

Parameter	Br t Ctr	Limb	N Arc	S Arc	E Arc	Faint
component	vpshock	vpshock	vpshock	vpshock	vpshock	vpshock
kT (keV)	$0.91^{+0.01}_{-0.03}$	$1.23^{+0.07}_{-0.05}$	$0.98^{+0.09}_{-0.08}$	$1.1^{+0.1}_{-0.1}$	$1^{+2}_{-0.2}$	$0.91^{+0.09}_{-0.01}$
Fe/Fe $_{\odot}$	$1.7^{+0.4}_{-0.3}$	$1.4^{+0.4}_{-0.2}$	$1.2^{+0.5}_{-0.4}$	$1.1^{+0.8}_{-0.3}$	$1^{+2}_{-0.5}$	$1.4^{+0.9}_{-0.4}$
τ (cm $^{-3}$ s)	$4^{+1}_{-3.6} \times 10^{13}$	$2.2^{+0.4}_{-0.2} \times 10^{11}$	$1^{+50}_{-0.4} \times 10^{12}$	$2^{+1}_{-1} \times 10^{11}$	$6^{+494}_{-5} \times 10^{11}$	$5^{+4}_{-2} \times 10^{11}$
norm (cm $^{-5}$)	$2.09^{+0.07}_{-0.07} \times 10^{-4}$	$2.0^{+0.1}_{-0.1} \times 10^{-4}$	$6.4^{+0.05}_{-0.04} \times 10^{-5}$	$3.8^{+0.03}_{-0.03} \times 10^{-5}$	$3.6^{+0.3}_{-0.4} \times 10^{-5}$	$4.3^{+0.3}_{-0.4} \times 10^{-5}$
χ^2_{red}	1.19	1.17	1.04	1.34	1.03	1.27
dof	91	177	54	44	36	57

Note. — Here and in Table 4, N_H is fixed at 3.4×10^{21} cm $^{-2}$ and non-Fe abundances at 0.3 solar. The “Limb” region incorporates the “Arc” and “Faint” regions.

Table 4. Best-fit spectral models to regions in Shell B

Parameter	Limb	Bright Ring		Faint Ctr	Hard Knot	
component	vpshock	vpshock	vpshock + pwr1w	vpshock	vpshock	vpshock + pwr1w
kT (keV)	$0.78^{+0.04}_{-0.05}$	$1.8^{+0.1}_{-0.2}$	$0.63^{+0.04}_{-0.03}$	$0.6^{+0.1}_{-0.1}$	$0.43^{+0.09}_{-0.06}$	$0.65^{+0.08}_{-0.09}$
Fe/Fe _⊙	$0.29^{+0.06}_{-0.07}$	$0.31^{+0.04}_{-0.05}$	$0.16^{+0.03}_{-0.04}$	$0.1^{+0.1}_{-0.1}$	$0.4^{+0.1}_{-0.1}$	0.3 ^a
τ (cm ⁻³ s)	$1.8^{+0.3}_{-0.3} \times 10^{11}$	$8^{+1}_{-1} \times 10^{10}$	$6^{+3}_{-1} \times 10^{11}$	$< 4 \times 10^{13}$	$< 4 \times 10^{13}$	$< 5 \times 10^{13}$
Γ	$2.2^{+0.4}_{-0.2}$	$2.6^{+0.4}_{-0.4}$
norm (cm ⁻⁵)	$4.6^{+0.3}_{-0.2} \times 10^{-4}$	$3.8^{+0.1}_{-0.1} \times 10^{-4}$	$8.3^{+0.4}_{-0.3} \times 10^{-4}$	$1.1^{+0.1}_{-0.2} \times 10^{-4}$	$5.1^{+0.3}_{-0.4} \times 10^{-5}$	$6^{+1}_{-1} \times 10^{-5}$
norm2 (cm ⁻⁵)	$6^{+1}_{-1} \times 10^{-5}$	$2.9^{+0.4}_{-0.3} \times 10^{-5}$
χ^2_{red}	1.22	1.26	1.05	0.80	1.29	1.08
dof	268	189	187	35	61	60

^aCould not be adequately constrained, so fixed to LMC mean abundance.

Table 5. SNR properties from spectral fits

	Shell A	Shell B
n_e (cm ⁻³)	$0.19 \pm 0.02 f_{\text{hot}}^{-1/2}$	$0.16 \pm 0.02 f_{\text{hot}}^{-1/2}$
M_{gas} (M _⊙)	$42 \pm 5 f_{\text{hot}}^{1/2}$	$100 \pm 10 f_{\text{hot}}^{1/2}$
E_{th} (erg)	$2.3 \pm 0.3 \times 10^{50} f_{\text{hot}}^{1/2}$	$3.6 \pm 0.4 \times 10^{50} f_{\text{hot}}^{1/2}$
P_{th} (dyn cm ⁻²)	$6.8 \pm 0.6 \times 10^{-10} f_{\text{hot}}^{-1/2}$	$3.9 \pm 0.4 \times 10^{-10} f_{\text{hot}}^{-1/2}$
v_{shock} (km s ⁻¹)	990 ± 10	820 ± 30
v_{exp} (km s ⁻¹)	740 ± 10	610 ± 20
t_{dyn} (yr)	7,400	13,000
t_{ion} (yr)	$46,000 f_{\text{hot}}^{1/2}$	$35,000 f_{\text{hot}}^{1/2}$

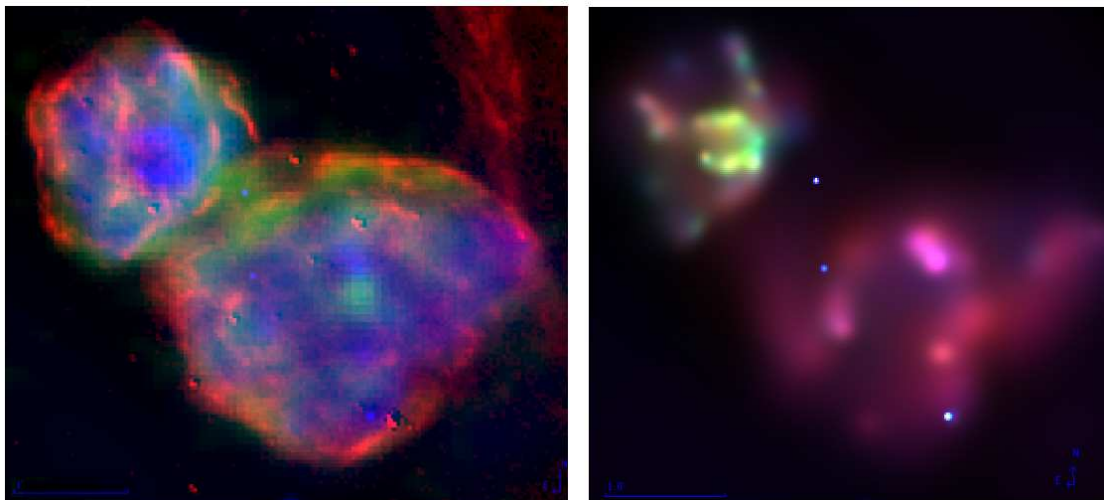


Fig. 2.— **Left:** 3-band image showing $H\alpha$ from the CTIO Curtis-Schmidt telescope (red), 7 cm radio map from the ATCA (green), and adaptively smoothed *Chandra* ACIS image (blue). **Right:** 3-color *Chandra* ACIS image showing emission at 0.3-0.8 keV (red), 0.8-1.5 keV (green) and 1.5-8.0 keV (blue). The X-ray images were adaptively smoothed on the same scale.

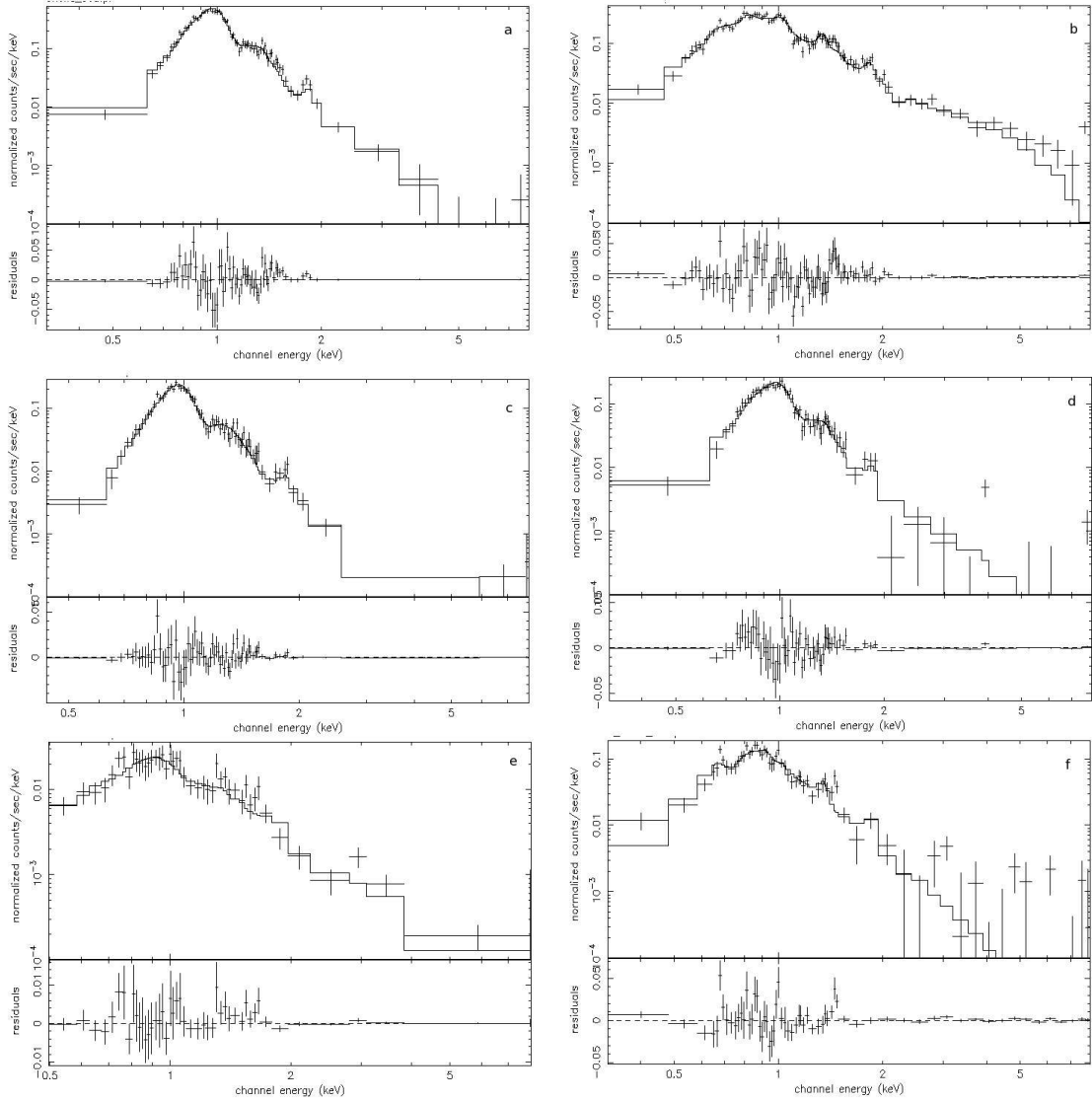


Fig. 3.— Spectral fits to *Chandra* ACIS data for: (a) Region 1, Shell A; (b) Region 2, Shell B; (c) Region 3, Shell A Bright Center; (d) Region 4, Shell A Limb; (e) Region 10, Shell B Hard Knot; and (f) Region 12, Shell B Limb.